Journal of Applied Fluid Mechanics, Vol. 18, No. 9, pp. 2268-2281, 2025.
Available online at www.jafmonline.net, ISSN 1735-3572, EISSN 1735-3645.
https://doi.org/10.47176/jafm.18.9.3351

A New Aspect of the Ground Effect: The Two-way Interactions between an Airplane Flying in the Vicinity of Sea Water and the Free Surface Waves

S. Eftekhari, A. R. Davari† and F. Pazooki

Department of Aerospace Engineering, SR.C., Islamic Azad University, Tehran, Iran

†*Corresponding Author Emails: ardavari@srbiau.ac.ir , ardavari@iau.ac.ir*

ABSTRACT

This study presents intensive numerical simulations of a general aviation airplane flying near a wavy water surface, considering the effects of ground proximity and wave amplitude on aerodynamic forces and moments. The Stokes third-order wave model was employed, and numerical results were validated using limited wind tunnel tests on a 3D-printed model, as well as existing NACA 4412 near-ground experimental data. Simulations for both flat and wavy surfaces reveal that above an elevation of h/c=1.5, aerodynamic coefficients remain similar to those near a flat surface. However, at lower clearances, aerodynamic responses exhibit strong oscillatory behavior, potentially leading to resonance and instability. The oscillations in lift (CL) and drag (CD) closely follow wave shape, while the pitching moment coefficient (Cm) shows a distinct phase lag. Large-amplitude waves significantly impact stability, leading to severe pitch oscillations, which may pose risks for aircraft flying near stormy sea surfaces. Contrary to the typically beneficial ground effect for wing-in-ground (WIG) aircraft, this study highlights the destabilizing influence of large surface waves in near-ground flight.

Article History

Received January 2, 2025
Revised March 25, 2025
Accepted April 16, 2025
Available online July 5, 2025

Keywords:

Ground effect
Downwash
Wavy water
Induced velocity
Venturi

1. INTRODUCTION

A Wing-in-Ground (WIG) effect aircraft flying in proximity to the ground experiences different flow phenomena compared to those operating in free stream (Qiu et al., 2014a). WIG aircraft typically fly near the water surface to avoid obstacles. Additionally, other types of aircraft, including commercial ones, may be required to land on the sea surface under certain emergency conditions (Yang & Wei 2010). Therefore, the ground effect problem should account for realistic wavy surface boundary conditions. While it is difficult to replicate such conditions in a wind tunnel, numerical simulations provide a more effective way to study wavy ground effects on WIG aircraft.

Despite numerous studies on airfoils and wings in ground effect, very few works in the literature focus on entire aircraft operating in ground effect, particularly near a wavy surface such as the sea. As an aircraft approaches the ground—whether wavy or smooth—both lift and the nose-down pitching moment increase. However, the lift-to-drag ratio depends not only on ground clearance but also on the angle of attack and may even decrease (Qiu et al., 2015; Haolin et al., 2019). In this case, the downwash flow from the wingtips is suppressed, weakening the wingtip vortices. As a result, the induced drag would decrease when the approaching the ground, while the parasite drag increases. Hiemcke (1997), Qiu et al. (2014b), and Li et al. (2015) independently found that the stall angle of attack for an airfoil decreases as the elevation from the ground decreases. When the elevation is reduced, the effective angle of attack experienced by the WIG increases, leading to a stronger spanwise flow on the wing. This, in turn, results in a thicker boundary layer at the wingtips. At sufficiently high angles of attack, separated flow dominates the upper surface. Consequently, as the WIG gets closer to the ground, the lift-to-drag ratio initially increases, reaching a maximum at a certain distance, and then starts to decrease as the vehicle continues to descend. Very close to the ground, the air beneath the vehicle is partially blocked and does not have enough space to pass through freely. This compressed air gives rise to the lower pressure on the vehicle and increases the lift. The increased pressure in this region is called the RAM pressure which is actually a dynamic air cushion under the WIG. The

NOMENCLATURE

v	kinematic viscosity	C_L	lift coefficient
h	airplane elevation from the water surface	C_D	drag coefficient
c	airplane overall length (characteristic length)	C_m	pitching moment coefficient
V_∞	free stream velocity	x	longitudinal axis pointed towards the airplane base
Re	Reynolds number=cV_∞/v	y	lateral axis pointed upward
H	wave amplitude	z	lateral axis pointed to the port side wing tip
L	wave length		

maximum CL is due to the wavy ground–induced RAM pressure and its minimum value is caused by the unusual suction pressure developed on the wing lower surface (Ahmed et al., 2007). Furthermore, when the vehicle is at a non-zero angle of attack, there would be an area contraction under the vehicle, i.e., the area between the lower surface and the ground surface creates a venturi effect which has a decisive role on the magnitude of lift developed on the airfoil (Quanbing et al., 2022). This causes a nonlinear behavior in aerodynamic coefficients at very small distances from the ground. When an aircraft flies over a wavy ground, the aerodynamic coefficients exhibit a periodic behavior and their amplitudes of variation increase at lower altitudes from the ground. The aerodynamic parameters increase when flying over a peak and decrease over a valley. The increase in CL and CL/CD in the proximity to the wavy surface is accompanied by a pitching moment enhancement that could lead to longitudinal instability (Boschetti et al. 2022). Some of the earliest numerical surveys have revealed that the amplitude of variations of lift and drag near a wavy surface strongly depends on the wave amplitude whereas the oscillation period in lift and drag variations depends on the surface wave length. Furthermore, the increase of lift with increasing wave amplitude near the surface, gives rise to the drag due to lift. However, irregular pattern for drag changes was observed when flying over a wavy surface.

Recently, Lee and Tremblay (2018) and Tremblay and Lee (2019) have performed several experiments on airfoils near a wavy ground surface. They have pointed out that there would be a periodic variation in the sectional lift and pitching moment while flying in the vicinity of a wavy wall, regardless of wave length and amplitude. These values were reported to increase as the distance to the ground decreases. They have also found that the impact of ground clearance on the aerodynamic behavior is more prominent than the wave amplitude. Apart from the airfoil, the problem of a wing in ground effect has also been the subject of various researches, and still is a pending topic in the literature (Araştırma et al., 2022).

Recently (Dreus et al., 2025) numerically analyzed an unmanned aircraft operating near a ship's surface for supply delivery. The results showed that the ground effect enhances aerodynamic performance by up to 1.5 times, enabling payload transport at speeds of up to 250 km/h with a takeoff weight of 2.7 tons. The computational analysis confirms that the proposed unmanned WIG craft is fully operational and holds promise for high-speed delivery of small payloads.

Şahbaz et al. (2019) conducted both numerical and experimental tests on an aircraft operating in ground effect. Their study investigates the rotary derivatives of an aircraft-type Wing-in-Ground (WIG) effect vehicle, which are essential for analyzing its stability and dynamics. The authors use Reynolds-averaged Navier–Stokes (RANS) equations to numerically predict these derivatives and validate their results against wind tunnel experiments. Their analysis accounts for the influence of ground clearance on aerodynamic coefficients and rotary derivatives. Additionally, the study highlights the challenges of wind tunnel testing, such as scale effects and model mounting influences, and provides recommendations for modeling aerodynamic characteristics in WIG vehicle stability studies. Even flow control methods have been implemented in this area. One study, conducted by (Methal et al., 2023), examined this topic. Their study explores the use of passive flow control to reduce induced drag in a Wing-in-Ground (WIG) craft by employing micro-vortex generators (MVGs) at a backward-facing step (BFS) location. The research addresses the issue of increased drag caused by the hull-fuselage design of WIG vehicles, which leads to inefficient fuel consumption.

The authors conducted both numerical and experimental analyses, testing MVGs of ramp type at various angles (12, 16, 24) and heights (0.4δ, 0.6δ, 0.8δ), where δ represents the boundary layer height. The models were fabricated using 3D printing and tested in a subsonic wind tunnel at Re = 6.1×10^4 to 6.1×10^5, with speeds ranging from 1 to 10 m/s.

This study provides insights into optimizing WIG craft aerodynamics to enhance fuel efficiency and overall performance.

As of yet, to the authors' knowledge, no survey has already been reported to engage with the problem of an entire airplane on water surface. This paper aims at the role of the sea water waves on aerodynamic behavior of an airplane operating near the water surface. A comprehensive numerical survey has been performed to study the role of the airplane elevation from the sea surface as well as the surface wave length and amplitude. Some wind tunnel tests have also been carried out on the same model near water to check the validity or the numerical analysis.

In the previous works on this issue a sinusoidal wave of constant shape has been considered above which, a 2-D airfoil was flying. This can simulate a solid ground. However, in the present paper, the waves on the water

surface have been examined in which the waves were propagating in the opposite direction of the airplane flight. In these simulations, using the existing two-phase models in Fluent, both the air and the water droplet phases have been engaged. As a result of wave motion and due to viscous dissipation, the wave broke down and its shape changed. Furthermore, the wave shape was distorted when the airplane passed over it.

2. THE APPROACH

The problem of a complete airplane near a wavy surface is too complex to check the grid independency or even choose a proper turbulence model. For this reason, the experimental data of an NACA 4412 airfoil in ground effect, Ahmed et al. (2007), have been re-produced numerically to check the effects of various turbulence models and also the type of the boundary conditions implemented in numerical algorithm. There is also some numerical data on the same airfoil in ground effect to be used as reference. The outcomes were employed in numerical analysis of the airplane flying in the vicinity of a wavy surface. A model for wind tunnel tests has also been produced using a 3-D printer. Several pressure taps were provided on the surface to measure the static pressure on some selected points on the model. The model was installed in a water tray with adjustable clearance during the wind tunnel test and the results were compared to those obtained by numerical simulations to approve the validity of the numerical results

3. THE MODEL AND EXPERIMENTAL APPARATUS

The specifications of the airplane model produced by 3-D printer for wind tunnel tests have been shown in Fig. 1. The same model was considered for the numerical simulation. Figure 2 shows the model along with the pressure taps provided on the surface. The model was placed on a water tray with an adjustable height. The non-dimensional clearance between the model and the water surface for the data presented in this paper was h/c=0.5. Shown in Fig. 3 are the model installed on adjustable strut on water tray. The wind tunnel test section measured 61 cm × 61 cm, with a maximum speed of 35 m/s, corresponding to a Mach number of approximately 0.1. The present experiments have been conducted far downstream of tunnel exit in the absence of wall interference and blockage effects, as shown in Fig. 4. The maximum velocity in the region behind the exit is approximately 20 m/s. The present experiments were conducted at free-stream velocities of 12 m/s, corresponding to Reynolds numbers of 2.2×10^5 and a Mach number of approximately 0.034.

4. THE NUMERICAL METHODOLOGY

In this paper, the unsteady, turbulent Navier-Stokes equations, coupled with the Volume of Fluid (VoF) method, are employed to simulate two-phase flow. Since the Mach number is less than 0.3, compressibility effects are neglected. The energy equation is also omitted because

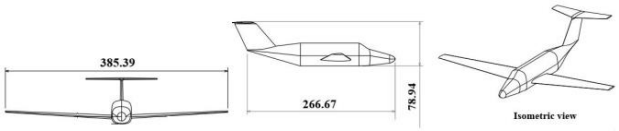

Fig. 1 Geometric parameters of the of the model

Fig. 2 Airplane model made by 3D printing along with the pressure taps

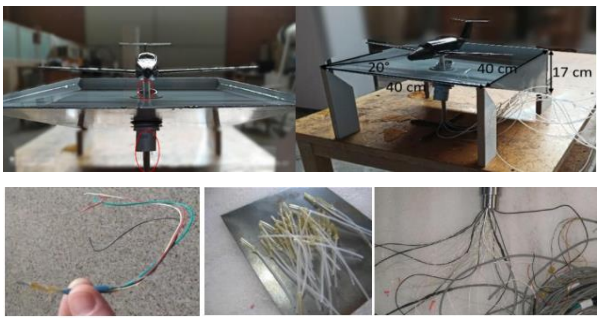

Fig. 3 Model installed on adjustable strut on water tray and the Kulite pressure sensors

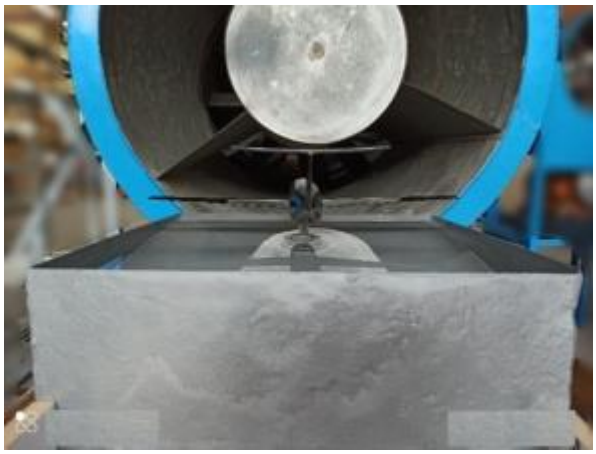

Fig. 4 Model along with the water tray installed downstream of the exit area

the aircraft's speed is low and does not exceed the sonic boom threshold, preventing shockwave formation and significant temperature increases that could affect the results. Phase transition does not occur in the subsonic region and has minimal impact even in the supersonic regime. Including it would only increase computational costs without significant benefits. The continuity and Navier-Stokes equations are given as follows:

$$\nabla . u = 0$$
$$\rho \frac{\partial u}{\partial t} + \rho \nabla .(uu) = \nabla .\left((\mu + \mu_t)\left(\nabla u + \nabla^T u\right)\right) - \nabla p + \rho g + F_\sigma \quad (1)$$

Here, u, p, ρ, μ and μ_t represent the velocity, pressure, density, viscosity, and turbulence viscosity, respectively. Additionally, g and F_σ denote gravity and the surface tension force between the two fluids. The VoF method introduces a variable, the volume fraction field α, which serves as an indicator determining the portion of a cell occupied by one of the two fluids. If α represents the fraction of the first fluid, then ρ_1 and ρ_2 are the densities of the two fluids. The density is then defined by the mathematical average as follows:

$$\rho = \alpha \rho_1 + (1 - \alpha)\rho_2 \quad (2)$$

Kinematic viscosity and other quantities are defined in the same manner. The Volume fraction, α is determined from Eq (3):

$$\frac{\partial \alpha}{\partial t} + \nabla .(\alpha u) = 0 \quad (3)$$

The turbulent model chosen for the current study is the k-ε RNG model. It consists of two equations, turbulence kinetic energy and dissipation rate which are as follows:

$$\frac{\partial}{\partial t}(\rho k) + \frac{\partial}{\partial x_i}(\rho k u_i) = \frac{\partial}{\partial x_j}\left[\left(\mu + \frac{u_t}{\sigma_k}\right)\frac{\partial k}{\partial x_j}\right] + P_k - \rho\epsilon \quad (4)$$

$$\frac{\partial}{\partial t}(\rho \epsilon) + \frac{\partial}{\partial x_i}(\rho \epsilon u_i) = \frac{\partial}{\partial x_j}\left[\left(\mu + \frac{u_t}{\sigma_\epsilon}\right)\frac{\partial \epsilon}{\partial x_j}\right] + C_{1\epsilon}\frac{\epsilon}{k}P_k - C_{2\epsilon}^{*}\rho\frac{\epsilon^2}{k}$$

Where**:**

$$C_{2\epsilon}^{*} = C_{2\epsilon} + \frac{C_\mu \eta^3 (1 - \eta/\eta_0)}{1 + \beta\eta^3} \quad (5)$$
$$\eta = Sk/\epsilon \text{ and } S = \left(2S_{ij}S_{ij}\right)^{1/2}$$

In this paper, the constants of the RNG model were set as:

The reason for selecting the RNG model is its heightened responsiveness to the effects of rapid strain and streamline curvature compared to the standard k-ε model. This characteristic explains the superior performance of the RNG model in the problem under consideration, Yakhot et al. (1992). First-order (Euler) time discretization was used, while second-order discretization was applied for spatial resolution. To solve the continuity and momentum equations, the implicit PIMPLE algorithm was employed, as the case is transient. The same discretization was used for volume fraction advection

4.1 The Mesh Configuration

For the CFD analysis, the model shown in Fig. 5 was created using FreeCAD and then imported into Pointwise for meshing. The optimal mesh for capturing gradients is a Cartesian mesh; however, due to the complexity of this case, tetrahedral elements were used instead. Tetrahedral meshes not only provide better connectivity to boundaries but also improve surface tension calculations in two-phase flow simulations.

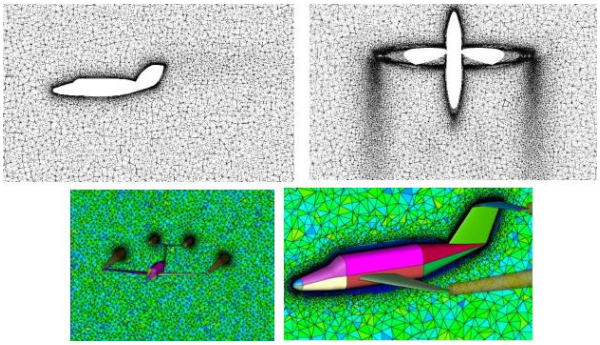

Fig. 5 Sections along the three Cartesian coordinate planes from the smaller domain including the airplane

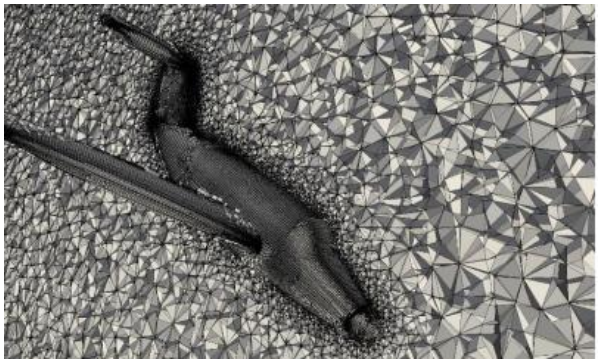

Fig. 6 The 3D view of the mesh

A boundary layer mesh was generated with a 0.7 mm gap between the first grid point and the body surface, corresponding to y+=30. Around the airplane, 50 layers of structured grids were created. Once the boundary layer grid points were established, they were connected to the outer domain's coarse grids using a combination of pyramidal and triangular elements. To accurately capture wingtip vortices, finer grids were generated in the wake region behind the wingtips, as illustrated in Fig. 5. Shown in Fig. 6 is the 3-dimensional view of the mesh structure.

To improve convergence, the mesh was constrained with a maximum skewness of 4, a maximum non-orthogonality of 65 degrees, and a maximum aspect ratio of 4.5.

4.2 The Computational Domain

To facilitate movement of the airplane, an advanced method involving an overset domain within a background mesh was utilized. This allowed to study how surface waves affect the airplane aerodynamic performance. As seen in Fig. 7, the overset domain (green boundaries) moves within the background mesh, with dimensions indicated to provide clarity on its spatial extent. A no-slip boundary condition was applied to the airplane surface within the overset region and the lower part of the background domain using Fluent software. In terms of boundary conditions, the inlet conditions were set for the left side of the background domain and outflow conditions for the other sides, ensuring an accurate numerical simulation.

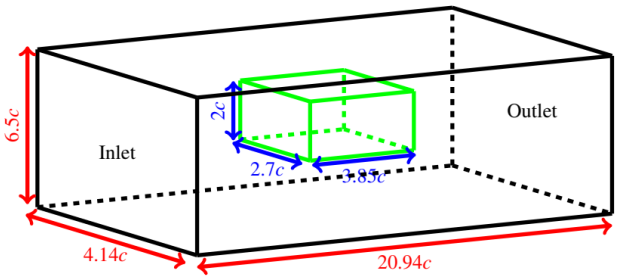

Fig. 7 Computational domain

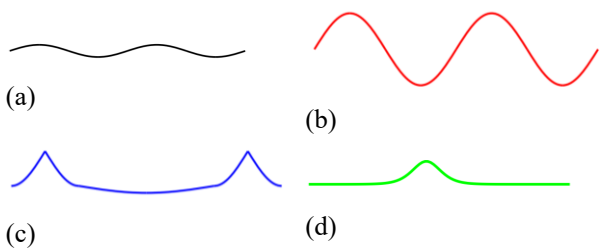

Fig. 8 Various wave shapes: (a) Airy Wave, (b) Stokes Wave, (c) Cnoidal Wave, (d) Solitary Wave

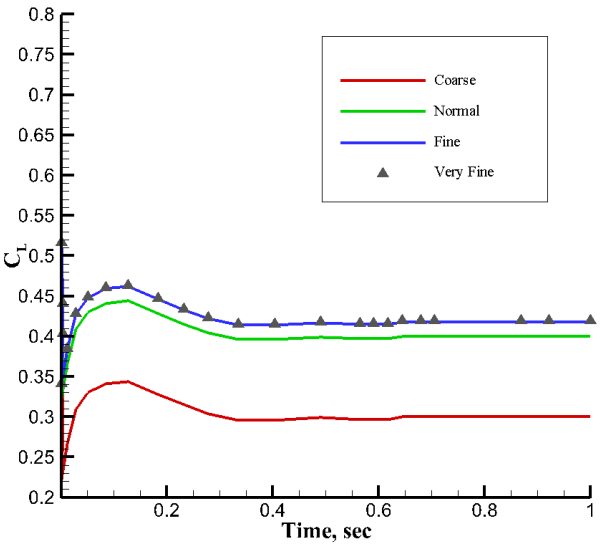

Fig. 9 Mesh independence study

4.3 The Surface Wave Modeling

Theories concerning surface water waves exhibit similarities to those governing wave propagation in material environments such as air. However, this study focuses on waves propagating along the boundary between water and air, rather than in a free boundary environment. The investigation is particularly interested in how waves distort and break down as the airplane passes over them. The surface water waves are generally categorized based on the ratio of wavelength to water depth, resulting in different wave shapes near the coast compared to further offshore. Notably, in deep water, the wavelength depends on the wave period, whereas in shallow water, it is affected by depth. In simpler linear wave theory, some assumptions are made, such as uniform depth and waves being treated as two-dimensional. Figure 8 illustrates different wave shapes according to wave theories24. Within the study, the focus is on the third order Stokes waves, which closely resemble real sea waves encountered by WIG craft. While it is unusual for aircraft to fly near deep water waves, WIGs commonly navigate intermediate or shallow depth water waves.

4.4 The Mesh Independency

To investigate the influence of mesh density on the results, the Lift Coefficient of the airplane model near a smooth sea surface was calculated using four different mesh types: coarse, normal, fine, and very fine. Simulations were performed for each mesh configuration under a uniform velocity of 12 m/sec with zero angle of attack. Figure 9 illustrates the variation of the Lift coefficient over time. The results indicate that refining the mesh beyond the fine level, equivalent to 714,840 cells, provides no significant improvement.

5. VALIDATION

Before the main simulations in this study, the k-ε RNG model and the VoF method for the numerical procedure are validated in this section. Two test cases were chosen for the validation, the first involves a single-phase flow around a NACA 4412 airfoil using the Navier-Stokes equations, while the second test case is the dam break problem- a benchmark for verifying two-phase flow models with the VoF method. Both simulations were performed using the k-ε RNG turbulence model.

5.1 The NACA 4412 Test Case

Flow around a NACA 4412 airfoil, taking the ground effect into account, was simulated using the k-ε RNG model with a chord length of 150 mm. The study includes a comparison between the numerical results obtained in this simulation and the experimental data of Ahmed et al. (2007), focusing on pressure, lift, and drag coefficients. Figures 10 and 11 demonstrate the satisfactory performance of the k-ε RNG model in predicting the aerodynamic coefficients for this airfoil at h/c=0.4 above the ground in comparison to the experimental data of Ahmed.

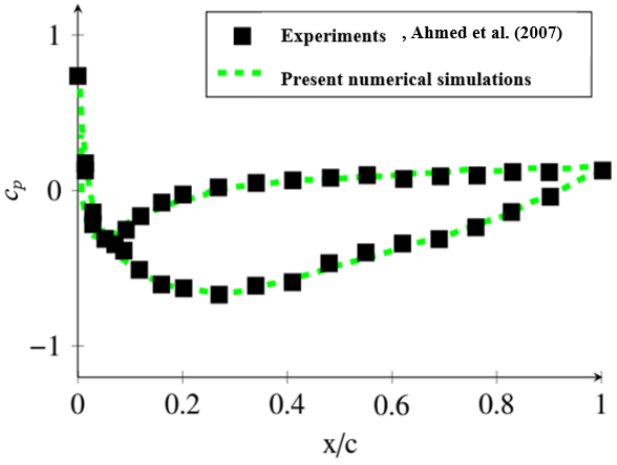

Fig. 10 Comparison of the present simulation with experimental data of Ahmed et al. (2007)

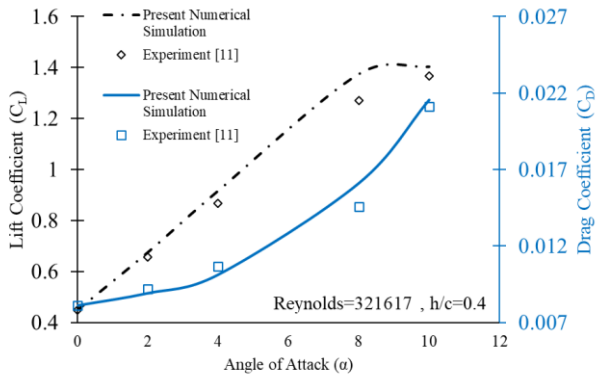

Fig. 11 Variations of lift and drag coefficients for NACA 4412 airfoil in comparison to the experimental data of Ahmed et al. (2007)

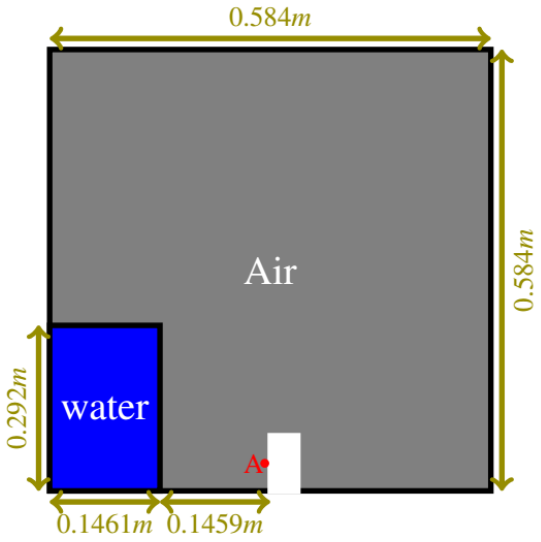

Fig. 12 Schematic sketch of the dam break simulation model, corresponding to the experiment, Issakhov et al. (2018)

5.2 The Dam Break Problem

In order to check whether the VoF method in the desired software is capable of accurately simulating two-phase flow, a widely used benchmark is employed for validation. The simplicity of the initial and boundary conditions makes it easy to verify numerical calculations. However, in most two-phase flow studies, experimental results are limited, and numerical simulations are often presented without direct experimental comparison. Figure 12 illustrates the geometry and the initial condition of the problem, Issakhov et al. (2018).

The dam break flow evolves through three discernible stages, as depicted in Fig. 13, showcasing snapshots derived from the simulation results, Koshizuka et al. (1995). In the first stage, the flow undergoes destruction and dispersion from the dam until the leading edge reaches the barrier. The second stage focuses on the interaction with the wall, including upward and downward fluid movements along the barrier, leading to interface connection due to backflow. Finally, the third stage encompasses the subsequent phase of the flow from connection to stabilization.

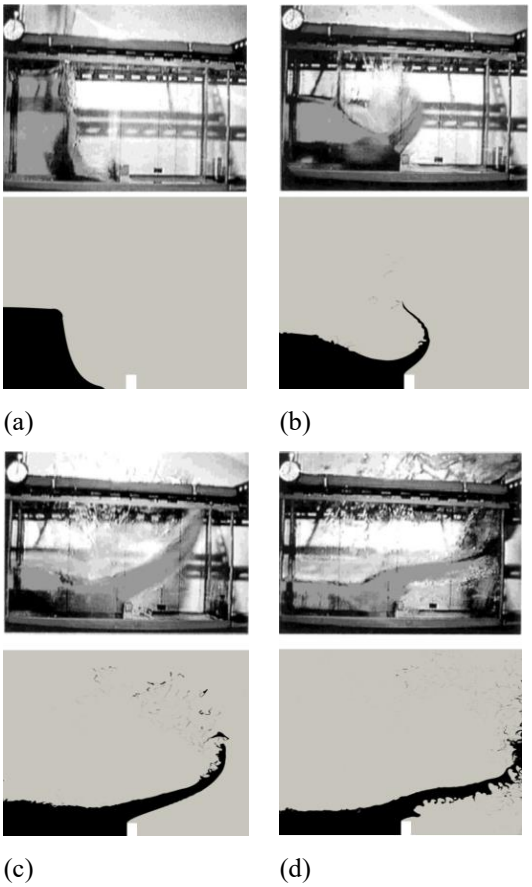

Fig. 13 Comparison of the general behavior of the fluid flow with experimental images after (a) 0.1, (b) 0.2, (c) 0.3 and (d) 0.4 seconds, Koshizuka (1995)

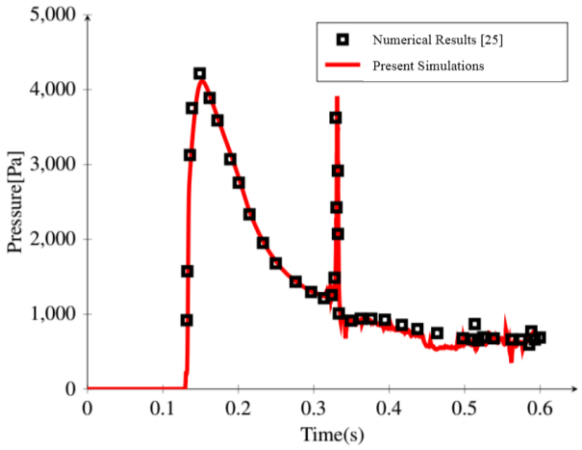

Fig. 14 Comparison of the pressure distribution at point A (shown in Fig. 12) with the numerical results of Issakhov

Figure 14 shows the pressure distribution at the marked point A in Fig. 12 performed by the authors using VoF, alongside the computational results from the study by Issakhov. Analysis of the numerical findings reveals anomalous pressure peaks attributed to the presence of the dam. The numerical simulation results for a dam break

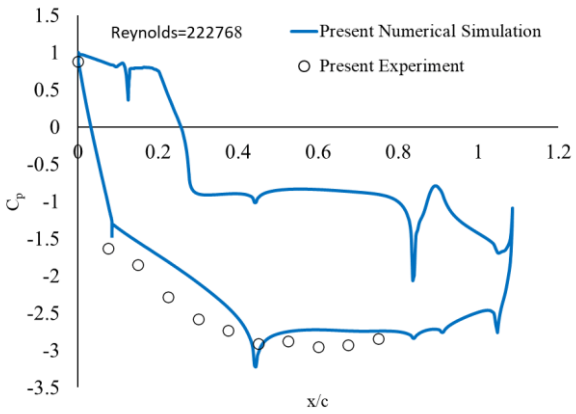

Fig. 15 Comparison between the pressure distributions on the upper surface of the airplane model obtained in wind tunnel and numerical simulation, at h/c=0.5

flow, depicting the dynamics of a gas-liquid mixture with a free boundary, exhibit favorable agreement with both the numerical data of Issakhov et al. (2018) and the experimental results of Koshizuka et al. (1995).

6. RESULTS AND DISCUSSIONS

To validate the numerical data, as stated earlier, a model manufactured by 3D printer has been tested near the water surface at the wind tunnel discharge to eliminate the wall and blockage effects on the results. The experiments were at a free stream velocity of 12 m/sec corresponding to a Reynolds number of 2.2×10^5 and at a vertical distance h/c=0.5 from water surface. The Kulite sensors, Fig. 3, were employed to measure the surface pressure on the model. Shown in Fig. 15 is the pressure distribution obtained in wind tunnel and that calculated from the present numerical simulation. On the lower surface, a mild acceleration is observed from the nose up to the beginning of the cylindrical fuselage at x/c=0.2, after which the flow field below the wing has reduced the pressure. Note that the lower surface flow is partially blocked by the ground effect. An interim recovery is evident from x/c=0.8 followed by another pressure drop due to tail boom and the venture- like effect in the vicinity of the water surface. The upper surface pressure is more affected by the fore body including the nose and the cockpit wind shield regions which has then been balanced by the wing flow field. The tail cone at the upper surface with a small ground effect, has caused a shallow recovery. According to this figure, the numerical data satisfactorily follows the experiments, though limited pressure taps have been provided on the wind tunnel model which was due to the restricted area inside to pass the connecting tubes to the pressure transducers. However, the average value of the discrepancy is less than about 10%.

Once the numerical data has been validated by the wind tunnel tests, the CFD simulations have been performed for the other cases, i.e., in the vicinity of both still and wavy water surfaces.

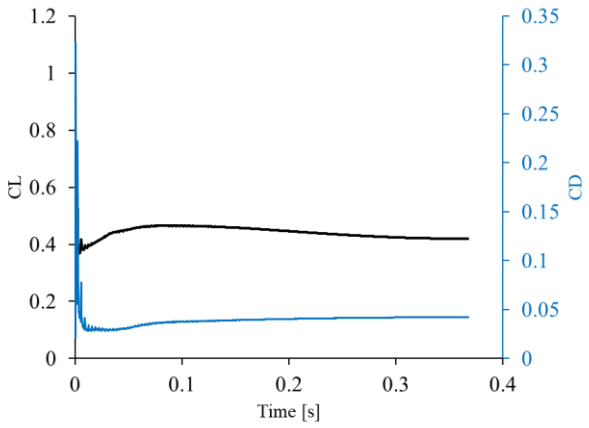

(a)

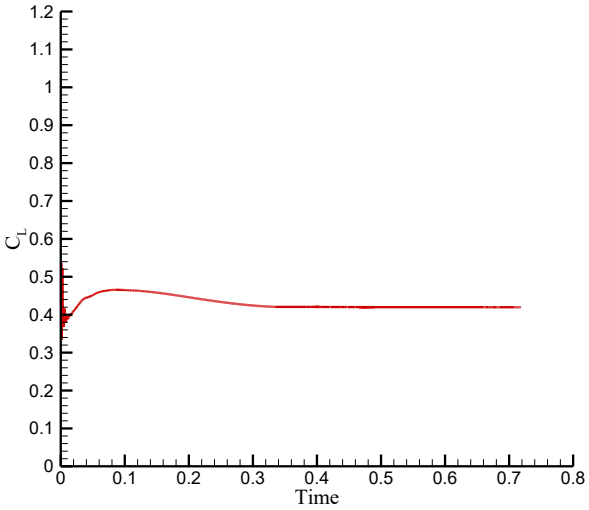

(b)

Fig. 16 The time variations of lift and drag for the airplane flying near the smooth surface, V∞=12 m/s (a) simulation time=0.3675 (b) simulation time=0.735

The numerical simulation time is a function of the field length and the airplane velocity. The distance between the inner moving domain including the airplane and the outer fixed domain was 4.41 m. Thus, with the airplane moving at V=12 m/sec, the total simulation time is 0.3675 sec. The length of each computational element in the direction of motion was 31.8 mm. In this direction 138 computational nodes were provided. The distance between the inner and the outer domains were divided into 1000 segments with a time step of 0.0003675 sec. This means that more than 10 time steps are required for each computational element.

Figure 16(a) shows the time variations of lift and drag for the airplane flying near the smooth water surface. The free stream velocity was 12 m/sec at zero angle of attack. It can be seen that the values of C_L and C_D have been converged to 0.439 and 0.0431 respectively which makes C_L/C_D=10.2. To check the solution convergence, the simulations were performed for a smooth surface so that it was allowed to continue up to 0.735 sec. The time variation of C_L is shown in Fig. 16(b) and illustrates a convergent behavior after t=0.3675.

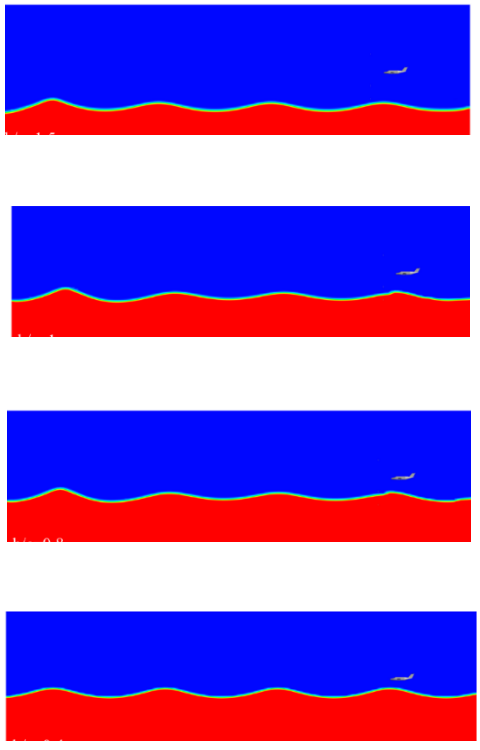

Fig. 17 Water-air interface for various airplane elevations, H/c=0.4, L/c=5, (a) h/c=1.5, (b) h/c=1.0, (c) h/c=0.8, (d) h/c=0.4

For the case of flying near the wavy surface, four elevations, h/c=0.4, 0.8, 1.0 and 1.5 have been examined. The wave amplitude and length were H/c=0.4 and L/c=5. The waves generated for the present calculations were the third order Stokes waves. The wave form and the airplane positions for the aforementioned elevations from the mean surface are shown in Fig. 17. In this figure the airplane flies from right to left and accordingly the waves are propagating from left to right to simulate the realistic flight conditions over a wavy sea. It shows wave breakdown as the plane moves to the left and also wave distortion as the airplane flies over it. The actual sea waves encounter breakdown as they propagate due to the interaction with air and the viscous dissipation. There are various criteria for the breakdown onset depending on the water depth and the wave length which has been summarized in wave theory text books[24].

The second, the third and the fourth order Stokes waves usually support wave breakdown and in the present paper the third order one has been considered to simulate this phenomenon which is as follows.

The surface elevation is given by (6)

$$\eta(x,t) = a\cos(kx-\omega t) + \frac{1}{2}ka^2\cos\big(2(kx-\omega t)\big) + \frac{3}{8}k^2a^3\cos\big(3(kx-\omega t)\big)$$

The velocity potential is expressed as: (7)

$$\phi(x,z,t) = \frac{a\omega}{k}e^{kz}\sin(kx-\omega t) + \frac{1}{2}\frac{a^2\omega}{k}e^{2kz}\sin\big(2(kx-\omega t)\big) + \frac{1}{3}\frac{a^3\omega}{k}e^{3kz}sin\big(3(kx-\omega t)\big)$$

where

a = wave amplitude

k = wave number

λ = wavelength

ω = wave angular frequency

x = horizontal position

z = vertical position

t = time

Third order stoke wave can cause a different behavior in variations of the forces and moments with time. In contrast to the existing results for a solid wavy wall which reported a periodic behavior in aerodynamic responses, in this paper, the upstream waves are original periodic but as they propagate, the breakdown occurs in wave shape and also the waves located under the airplane are distorted due to the flowfield below the moving airplane, especially when it is in the close proximity to the water surface.

In the present paper, the simulations were performed for intermediate deep waves which are more similar to the actual circumstances the airplane usually experience. Note that very close to the coast, the waves have high amplitudes, short lengths and small velocities which are not convenient and safe to fly over. Very far from the coast in deep water, the unpredictable high wind speed can cause abrupt wave break down and the phenomenon would be remarkably sophisticated to analyze and model.

Variations of the longitudinal aerodynamic responses with time, as the airplane flies over the wavy water have been shown in Fig. 18. The wave amplitude and length were constant and the calculations have been performed at four elevations h/c=0.4, 0.8, 1.0 and 1.5. When the airplane flies near the wavy surface, the lift and drag also exhibit a wavy behavior. Secondly both coefficients increase as the elevation from the surface decreases. Moreover, the oscillatory behavior of lift and drag diminishes as increasing the elevation. The average values of C_L and C_D at h/c=1.5 i.e. far from the wave surface, are 0.449 and 0.042, respectively which are very close to those pointed out in Fig. 16 for the smooth water surface.

When decreasing the elevation, h/c, both C_L and C_D increase due to the ground effect. Again, to check the solution convergence, the simulation time for a single case of h/c=0.8 was extended up to 0.735 sec and the result, shown in Fig. 18(b), approves the convergent behavior after t=0.3675.

Table 1 indicates the average values of C_L, C_D and C_L/C_D from Fig. 18 for various h/c. It can be inferred that when flying at h/c=1.5 above a wavy surface, the mean aerodynamic forces are very close to those corresponding to a smooth surface. The subtle oscillations in this case can

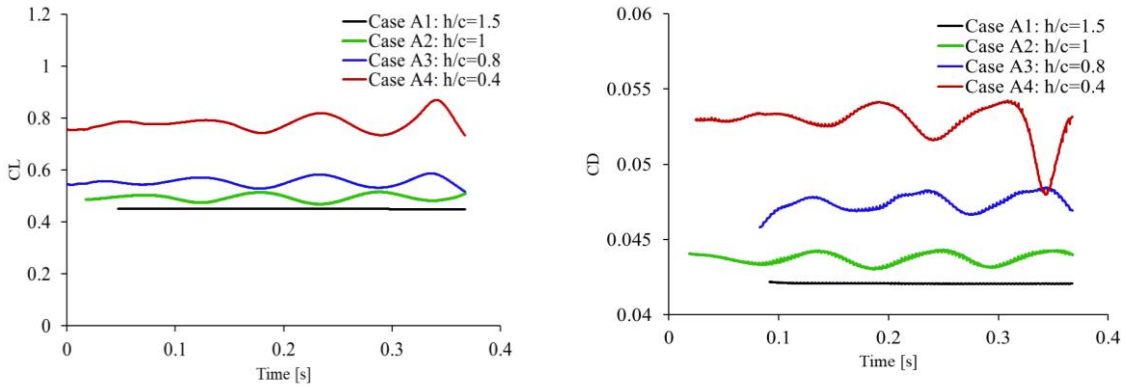

(a)

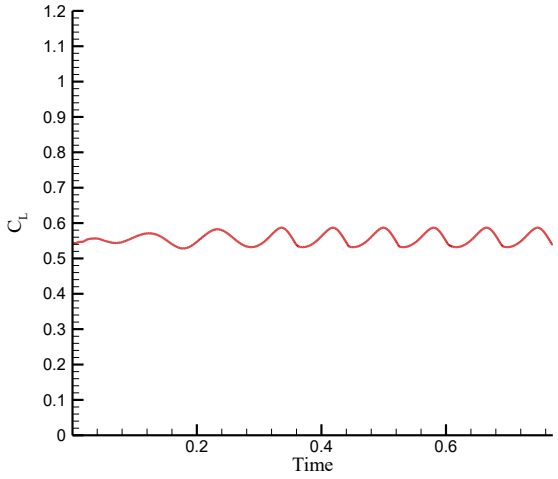

(b)

Fig. 18 (a) Variations of lift and drag at different elevations for H/c=0.4 and L/c=5 for a simulation time of 0.3675, (b) Variations of CL at h/c=0.8 for an extended simulation time of 0.735

Table 1 The k-ε RNG coefficients

Cμ	σk	σε	C1ε	C2ε	η0	β
0.0845	0.7194	0.7194	1.42	1.68	4.38	0.012

easily be taken care by a control system in airplane. Note that C_L/C_D for h/c=1.5 is still higher than that in the absence of ground effect and could be advantageous during an emergency landing on water. As descending to h/c=1.0, 0.8 and lower, not only the average values of the aerodynamic coefficients increase, but also increases the fluctuation level in the aerodynamic responses which can lead to large uncontrollable oscillations in the airplane.

The velocity contours in Fig. 19 explain the oscillations of C_L and C_D as the airplane flies over the wavy surface for the values of h/c=1.5 and 0.4. According Fig. 19(a) the waves impart less disturbances to the airplane at h/c=1.5 comparing to h/c=0.4. When flying at h/c=0.4, Fig. 19(b), some low-speed regions can be observed before and after each peak above the wave which are the signature of the venturi effect on the flow between the airplane lower surface and the wavy surface of water. As the airplane passes over the top of the wave, the ground effect, i.e., the blockage between the wave and the lower surface of the airplane would be more prominent which

Table 2 Table 2 The average values of the aerodynamic parameters

h/c	C_L	C_D	C_L/C_D
1.5	0.45	0.042	10.6
1.0	0.49	0.043	11.2
0.8	0.55	0.046	11.95
0.4	0.78	0.052	14.95

results in a local increase in C_L. On the other hand, while flying over the bottom of the waves toward the top, a gradual area contraction occurs and C_L decreases comparing to its mean value.

This figure shows that the maximum values of C_L as well as the minimum values of C_D occurs when flying over the top of the wave surface. Consequently, 180 degrees phase difference can be observed between the variations of C_L and C_D with time. The increase in C_D over the valleys is likely to be related to the suction effect. Note the surface wave shape in 3D view in Fig. 19(c) where the

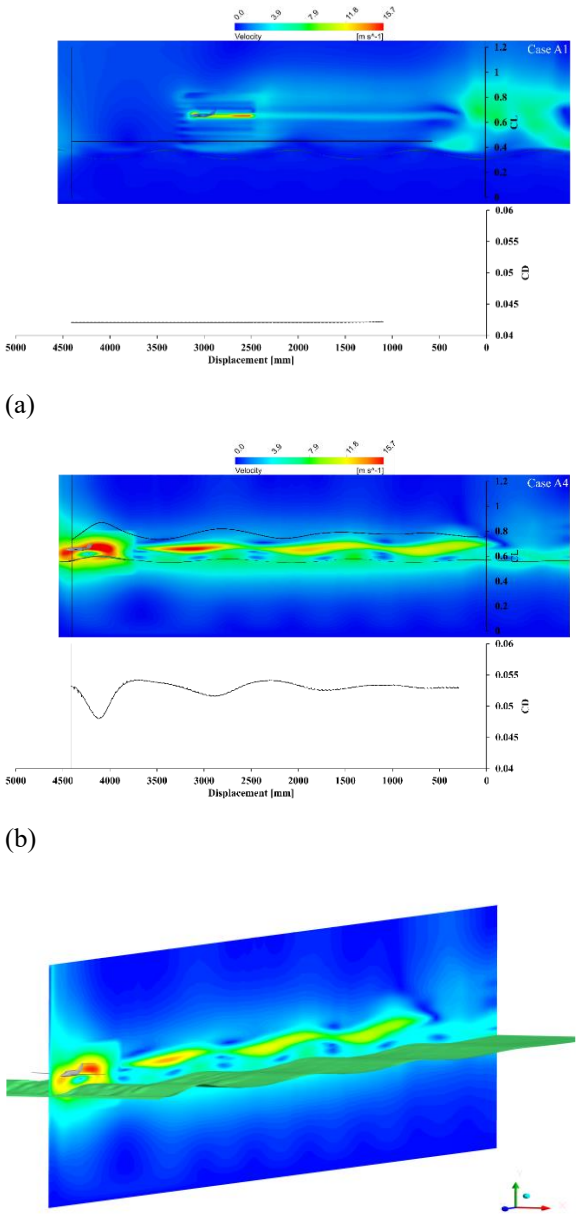

Fig. 19 The longitudinal velocity contours in the plane of motion of the airplane as it flies over the wavy surface, (a) h/c=1.5 (b) h/c=0.4 (c) the 3D contour showing the wave surface pattern

disturbances on wave surface due to the airplane flowfield and also the wave break down as the waves propagate to the right can be clearly observed.

The time variations of C_L and C_D were transferred into frequency domain by Discrete Fourier Transformation, DFT, to point out the relationship between the surface wave shape and the aerodynamic responses. Figure 13 shows the power amplitudes of C_L and C_D in frequency domain. The major frequency mode for the wave shape is at f=8.8 Hz, corresponding to the wave frequency. The next harmonies are the factors of this frequency in the form of n×f where n is 2, 3, 4, etc.

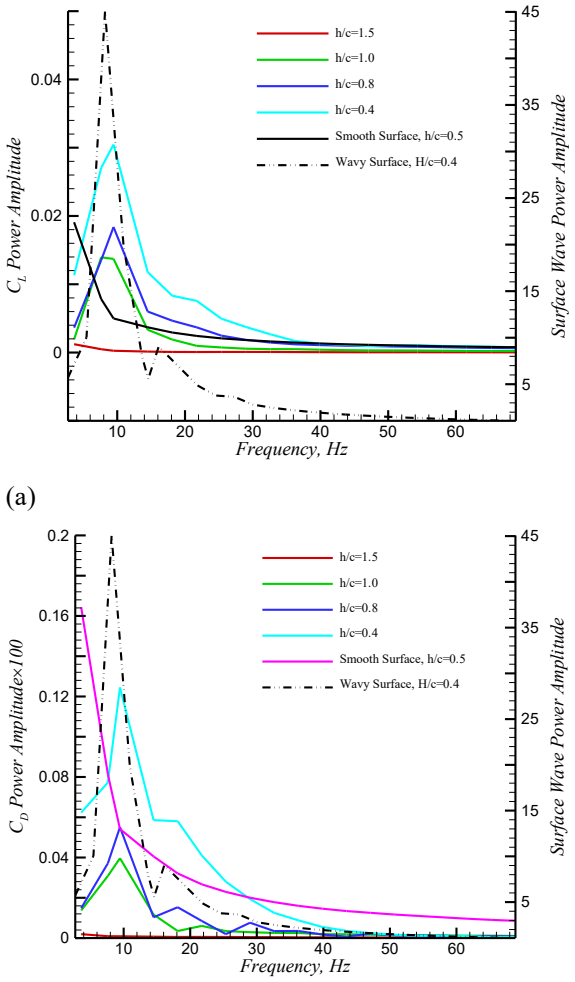

Fig. 20 The power spectrum density for various elevations from the wave surface, (a) C_L (b) C_D

It can be seen by inspection that the dominant frequency in variations of C_L and C_D near the surface, i.e., h/c=1.0, 0.8 and especially 0.4 is the same as the wave shape. The sensitivity of C_L to variations of the wave surface decreases as increasing the elevation, h/c which is evident from decreasing the power amplitude as h/c increases. However, when flying out of ground effect at h/c=1.5, a monotonic behavior in power spectrum is observed, either does the smooth surface behave. In the latter case, there are very small amplitude oscillations in frequency modes, showing that the forces do not have any significant variations with time when flying over a smooth surface. From Fig 20(b) one can see that the dominant frequency for C_D is slightly higher than the wave frequency. This suggests that the surface wave has different effects in the flight direction and perpendicular to it. Furthermore, several lower amplitude frequency modes can also be observed in the power spectrum of C_D that might the signature of viscosity which is more prominent in drag coefficient.

To study the effects of the wave height on the aerodynamic behavior, more simulations have been performed for the wave amplitudes of H/c=0.2, 0.3, 0.4 and 0.5 while the airplane was flying at an elevation h/c=1

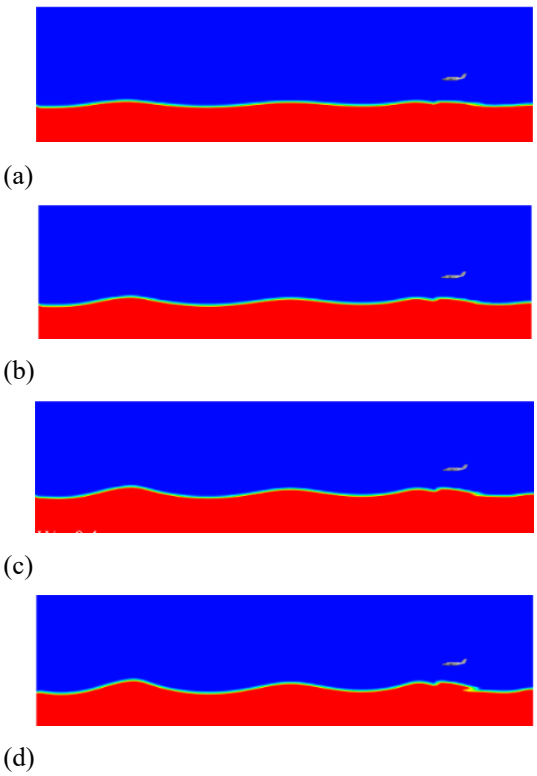

Fig. 21 Water-air interface for various wave amplitudes, h/c=1, L/c=6.5. (a) H/c=0.2, (b) H/c=0.3, (c) H/c=0.4, (d) H/c=0.5

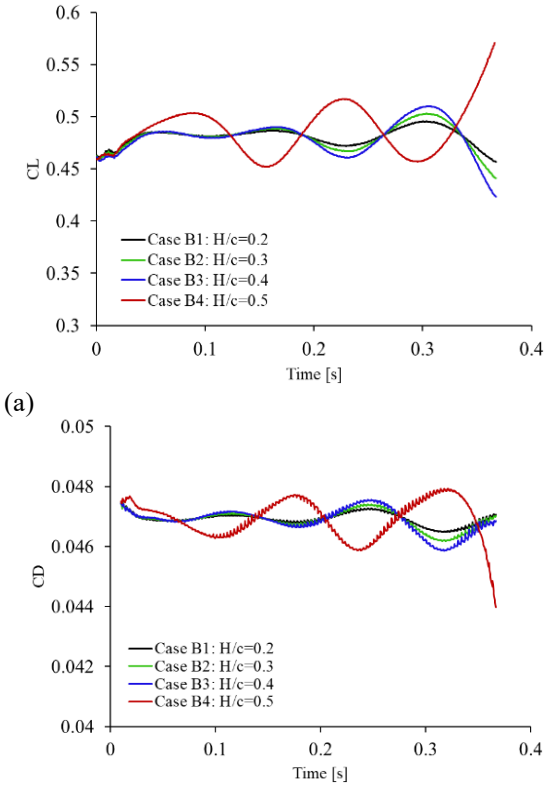

Fig. 22 Variations of lift and drag at different elevations for h/c=1 and L/c=6.5

above the wavy surface. The wave length was set to a constant value of L/c=6.5. Figure 21 shows the shape of the surface waves after 300 time steps when the waves are fully developed. Again, the wave pattern changes as it propagates to the right and the airplane also imparted another change in wave shape due to its flowfield.

Shown in Fig. 22 are the time variations of C_L and C_D as the airplane flies over the wavy surface. It can be seen by inspection that the average values of C_L and C_D are 0.48 and 0.046, respectively and are nearly independent of the amplitude, since the airplane elevation from the mean surface remains constant with wave amplitude.

Further, note that, in contrast to Fig. 18, the time variations of C_L and C_D in Fig. 22 follow the surface wave shape for all amplitudes. As stated earlier, when flying at h/c<1, the time variations of aerodynamic behavior are very different from the wave shape. For the case of flying with various elevations over a constant amplitude wave, as the airplane gets closer to the wavy surface, the average values of C_L and C_D increase and the oscillations in these coefficients as the airplane flies over the surface are also amplified. With these in mind, to study the effects of the wave amplitude, the airplane height above the average wave level was set to a constant value of h/c=1.0. For this reason, no remarkable difference can be seen in the time variations of C_L and C_D for different amplitudes. However, the oscillations in C_L and C_D, which are amplified with time, are the signature of the Stokes waves on the water surface.

As the wave amplitude increases from H/c=0.2 to H/c=0.4, a minor increase can be pointed out in the

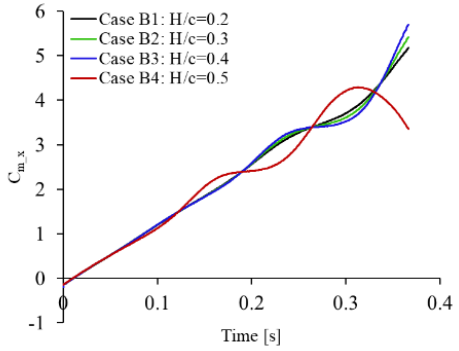

Fig. 23 Time variations of the pitching moment for various wave amplitudes at L/c=6.5 at an elevation h/c=1

amplitude of oscillations in C_L and C_D. However, when the wave amplitude is increased to H/c=0.5, a dramatic increase in the amplitude can be seen. Note that the top of the waves gets too close to the airplane at this amplitude. On this basis, flight over the waves of the amplitudes larger than H/c=0.4 should be at the elevations higher than h/c=1, otherwise the airplane stability would remarkably decrease.

The time variation of the pitching moment for the wave amplitudes H/c=0.2, 0.3, 0.4 and 0.5 while the airplane was flying at an elevation h/c=1 above the wavy surface is shown in Fig. 23. The model center of gravity was located at 52% of the body length. Among the longitudinal aerodynamic coefficients, C_L and C_D are more affected by the surface wave than the pitching

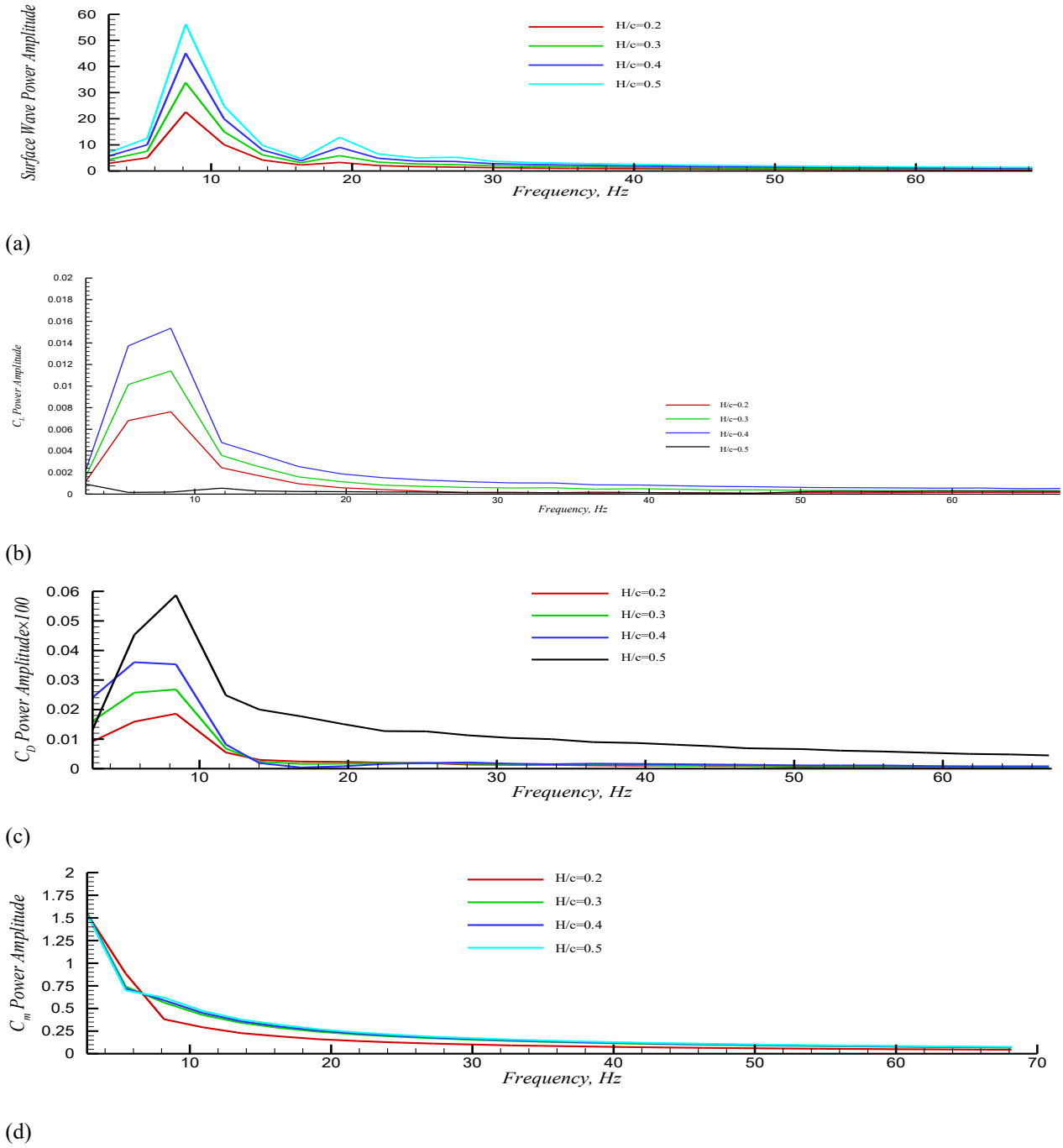

Fig. 24 Power spectrum density for various wave heights and a constant airplane elevation of h/c=1.0, (a) Wave surface, (b) C_L, (c) C_D, (d) C_m

moment coefficient, C_m. However, in contrast to C_L and C_D, the absolute value of the mean C_m changes with wave amplitude.

Accordingly, regardless of the shape of the waves, the fluctuations around the mean and the other parameters involved in this problem, if the plane is close enough to the sea surface, e.g., h/c<1.5, the waves will always have an adverse impact on airplane nose deviation and the longitudinal stability. On the other hand, when flying at low altitudes, e.g., h/c<0.5 over high amplitude surface waves, in particular for H/c>0.5, in addition to remarkable variations in C_L and C_D, severe fluctuations would also occur in airplane pitch attitude which can lead to entire loss of stability. Figure 22 suggests that the airplane is statically stable, i.e., it has an initial tendency to overcome the perturbations and recover its stable conditions. However, the successive waves impart periodic disturbances which in the absence of a flight control system may lead to dynamic instability, though it could not be observed in the present data. This can explain the drag behavior in Fig. 22. Drag encompasses the induced and the parasite parts. The ground proximity decreases the induced part and consequently the total drag is expected to decrease, while an opposite behavior is seen. The pitching moment is observed to continuously increase in the absence of an active control system to compensate the periodic lift changes. As a consequence, the pitch attitude

increases and a greater area of the airplane would be exposed to the oncoming air which in turn gives rise to the parasite drag. Thus, despite decreasing the induced drag, the total drag increases near the ground as a result of an increase in parasite drag.

Various wave amplitudes, for a constant wave length, have been shown in frequency domain in Fig. 24(a). The higher the wave amplitude, the higher will be the amplitude of the dominant wave frequency, i.e. f=8.8 Hz and its consequent harmonies. Shown in Fig. 24(b), (c) and (d) are the variations of C_L, C_D and Cm power amplitudes in frequency domain, respectively. As the wave height, i.e., H/c, increases, the amplitude of the dominant frequency mode in C_L power spectrum also increases, while the dominant frequency is still f=8.8 Hz. This shows that the sensitivity of the C_L variation to the surface wave increases at higher wave heights. For H/c=0.5, which is the highest wave, variations of C_L in frequency domain show a weak response. This implies that the time variations of C_L, as the airplane flies near a high-amplitude wave, does not follow the wave shape and exhibit a nearly independent behavior, though being affected by the surface wave. In contrast to C_L, Fig. 24(c) shows that C_D exactly follows the wave amplitude even at H/c=1.5 where C_L, has already been shown to exhibit no remarkable response. This shows that despite both C_L and C_D are sensitive to the wave elevation, in flight near the highest amplitude wave, e.g., H/c=0.5, the variations of C_L do not follow the surface wave height while C_D still continues to follow it. This difference again suggests that the lift and drag receive the surface wave effect in different manners or mechanisms.

The power spectrum for the pitching moment also reveals an interesting fact. The Fourier transform of the pitching moment in frequency domain show a monotonic behavior regardless of the wave shape and amplitude, even though for higher wave amplitudes, the magnitude of the transformed C_m slightly increases so that the transformed Cm for the lowest amplitude wave is completely distinguished among the rest for the higher amplitude surface waves. However, this monotonic behavior shows that the pitching moment oscillations when flying over the wavy surface does not have any signature from the surface wave shape and exhibits irregular fluctuations. Such fluctuations, as stated earlier, can sometimes be out of control and may lead to remarkable airplane instability near the stormy sea surface.

7. CONCLUSION

Intensive numerical simulations have been carried out on a scaled model of a general aviation airplane flying near the water wavy surface. The Stokes third order wave shape has been considered and the effect of ground proximity as well as the wave amplitude has been investigated on airplane 2D longitudinal forces and moment. Some limited wind tunnel tests have also been performed on the same model, manufactured by 3D printing method, in the vicinity of water surface to validate the numerical results. The experimental data of NACA 4412 near the ground, reported in the literature, was employed to check the numerical settings for the present calculations. The numerical simulations were performed both for flight over a flat surface and over a wavy surface. The results show that above an elevation h/c=1.5 from the wavy surface, the mean values of the aerodynamic coefficients are nearly the same as those for flying near a flat surface. On the other hand, for very close clearance between the airplane and the wavy surface, the aerodynamic responses are strongly affected by the surface wave shape and exhibit a diverging oscillatory behavior, which may lead to resonance and loss of stability. According to the present results, the oscillations in aerodynamic coefficients are strong functions of the wave amplitude and the time variations of C_L and C_D nearly follow the shape of the surface wave, though it does not have any remarkable effect on the mean values of C_L and C_D. It has found that the dependency of oscillations in C_D to the surface wave shape is somehow different from that for C_L. The moment coefficient, C_m has also been observed to show a monotonic behavior in frequency domain which means that the time oscillations of C_m during flight above the wavy surface, unlike C_L and C_D, is not in-phase with the wave shape. However, the large-amplitude waves have significant impact on both the fluctuations and mean values of C_L, C_D and C_m, that may cause severe longitudinal instability near a stormy sea surface. Despite the ground effect is usually favorable for WIG aircraft, it has been worked out that the combination of near-ground flight and large-amplitude surface waves, not only is not advantageous, but also remarkably increases the pitch attitude oscillations and may result in sever instability.

CONFLICT OF INTEREST

The authors declare that they have no conflicts to disclose.

AUTHORS CONTRIBUTION

S. Eftekhari performed the numerical and experimental simulations. **A. R. Davari** has arranged the simulation scenarios and directed the entire process and prepared the manuscript. **F. Pazooki** has edited the manuscript.

REFERENCES

Ahmed, M. R., Takasaki, T., & Kohama Y. (2007). Aerodynamics of a NACA4412 airfoil in ground effect. *AIAA Journal*, *45*(1), 37–47. https://doi.org/10.2514/1.23872.

Araştırma, M., Ozdemir, H. Y., & Taner, C. (2022). The influence of turbulence models on the numerical modelling of a 3D wing in ground effect. *European Journal of Science and Technology*, *43*(43), 86–90. https://doi.org/ 10.31590/ejosat.1200056.

Boschetti, P. J., Neves, C. A., & González, P. (2022). Nonlinear aerodynamic model in dynamic ground effect at high angles of attack. *Journal of Aircraft*, *15*(6). https://doi.org/10.2514/1.C036721.

Dreus, A., Alekseyenko, S., Kulyk, O., & Nekrasov, V. (2025). Prospects for the creation of small-sized high-

speed unmanned aerial vehicles based on WIG-craft. EUREKA: *Physics and Engineering*. 1 (Jan. 2025), 34-43. https://doi.org/10.21303/2461-4262.2025.003308.

Haolin, Z., Tianhang, X., Jichang, C., Bin, W., Mingbo, T., & Zhenhao, Z. (2019). Numerical analysis of aerodynamics of a naca4412 airfoil above wavy water surface. *AIAA Aviation Forum*, 1–29. https://doi.org/10.2514/6.2019-3694.

Hiemcke, C. (1997). *NACA 5312 in ground effect - Wind tunnel and panel code studies.* 15th Applied Aerodynamic Conference. https://doi.org/10.2514/6.1997-2320.

Issakhov, A., Zhandaulet, Y., & Nogaeva, A. (2018). Numerical simulation of dam break flow for various forms of the obstacle by VOF method. *International Journal of Multi-phase Flow*, *109*, 191-206. https://doi.org/10.1016/j.ijmultiphaseflow.2018.08.003

Koshizuka, S., Oka, Y., & Tamako, H. (1995). *A particle method for calculating splashing of incompressible viscous fluid (No. CONF-950420-)*. American Nuclear Society, Inc., La Grange Park, IL (United States).

Lee, T., & Tremblay-Dionne, V. (2018). Experimental investigation of the aerodynamics and flowfield of a NACA 0015 airfoil over a wavy ground. *Journal of Fluids Engineering Trans ASME*, *140*(7). https://doi.org/10.1115/1.4039236.

Li, S., Zhou, D., Zhang, Y., & Qu, Q. (2015) Aerodynamic investigation of RAE2822 airfoil in ground effect, *Procedia Engineering*, 126, 174-178. https://doi.org/10.1016/j.proeng.2015.11.208

Methal, Z., Talib, A. S. A., Bakar, M. S. A., Rahman, M. R. A., Sulaiman, M. S., & Saad, M. R. (2023). Improving the aerodynamic performance of wig aircraft with a micro-vortex generator (MVG) in Low-Speed Condition. *Aerospace, 10*, 617. https://doi.org/10.3390/aerospace10070617

Qu, Q., Jia, X., Wang, W., Liu, P., & Agarwal, R. K. (2014a). Numerical study of the aerodynamics of a NACA 4412 airfoil in dynamic ground effect. *Aerospace Science and Technology*, *38*, 56–63. https://doi.org/10.1016/j.ast.2014.07.016.

Qu, Q., Lu, Z., Liu, P., & Agarwal, R. K. (2014b). Numerical study of aerodynamics of a wing-in-ground-effect craft. *Journal of Aircraft*, *51*(3), 913–24. https://doi.org/ 10.2514/1.C032531.

Qu, Q., Wei, W., Liu, P., & Agarwal, R. K. (2015) Airfoil aerodynamics in ground effect for wide range of angles of attack. *AIAA Journal*, *53*(4), 1048–1061. https://doi.org/10.2514/1.J053366.

Quanbing, S., Shi, Z., Zhang, W., Sun, Z., & Chen, Y. (2022). Numerical simulation of ground effect on circulation control airfoil. *International Journal of Aerospace Engineering*, https://doi.org/10.1155/2022/4985193.

Şahbaz, M., Sezer Uzol, N. and Kurtulus, D. (2019). *Numerical and Experimental Investigation of Rotor Aerodynamics in Ground Effect with Inclined Planes*. The 8th Asian/Australian Rotorcraft Forum (ARF 2019), Ankara, Turkey.

Tremblay-Dionne V., & Lee T. (2019). Experimental study on effect of wavelength and amplitude of wavy ground on a NACA 0012 airfoil. *Journal of Aerospace Engineering,* *32*(5), https://doi.org/10.1061/(ASCE)AS.1943-5525.0001051.

Yakhot, V. S., Orszag, S. A., Thangam, S., Gatski, T. B., & Speziale, C. (1992). Development of turbulence models for shear flows by a double expansion technique. *Physics of Fluids A: Fluid Dynamics*, *4*(7), 1510-1520.

Yang, Z., & Wei, Y. (2010). Complex flow for wing-in-ground effect craft with power augmented ram engine in Cruise. *Chinese Journal of Aeronautics*, 1–8. https://doi.org/10.1016/S1000-9361(09)60180-1.